MODELING SUSPENDED SEDIMENTS IN AMAZON FLOODPLAINS USING ORBITAL MODERATE RESOLUTION SENSORS

Daniel Andrade Maciel[1], Rogério Flores Jr.[1], Carolline Tressmann Cairo[1], Lino Augusto Sander de Carvalho[3], Felipe de Lúcia Lobo[1], Felipe Menino Carlos[1], Vitor Souza Martins[2], Cláudio Clemente Faria Barbosa[1], Evlyn Márcia Leão de Moraes Novo[1],

[1]Instituto Nacional de Pesquisas Espaciais; Av. dos Astronautas, 1.758 - Jardim da Granja, São José dos Campos - SP, 12227-010; damaciel_maciel@hotmail.com; rogerio.floresjr@gmail.com; carolline.cairo@inpe.br; felipellobo@gmail.com; felipe.carlos@fatec.sp.gov.br; claudio.barbosa@inpe.br; evlyn.novo@inpe.br; [2]Iowa State University – ISU. Caixa Postal 50011 – Ames – Iowa, United States, vitorstmartins@gmail.com; [3]Universidade Federal do Rio de Janeiro, Departamento de Meteorologia, lino.sander@gmail.com

ABSTRACT

Remote sensing (RS) images can improve the knowledge on the exchanges of sediment between the main rivers and floodplains as it provides a synoptic view of water bodies, at local and regional scales. The monitoring of total suspended solids (TSS) is important because the proportion of organic to inorganic particles varies in time and space and is linked to biogeochemistry of floodplain environments. Moreover, this proportion maybe affected by climate change as well as land use and land cover change. In order to grasp the spatial distribution of suspended sediments in Amazon Floodplains lakes, we have applied Monte Carlo simulation for calibrating several empirical and semi-analytical algorithms to estimate TSS based on in-situ Rrs and TSS concentration measured between 2015-2017. Calibrated models were then applied to atmospheric corrected Landsat/8, Sentinel 2-A, and CBERS-4 scenes. The results showed that is possible to estimate TSS on the floodplains using these three satellites, with errors lower than 30%.

Key words *— Curuai Lake, CBERS, Landsat, Sentinel, TSS.*

1. INTRODUCTION

Amazon Floodplains play an essential role in the biogeochemical cycle of the Amazon River Basin, altering the transport of particulate and dissolved matter as the Solimões/Amazon River flows towards the Atlantic Ocean [1]. These biogeochemical processes are influenced by both hydrological and Land Use/Land Cover Change (LUCC) processes at several spatiotemporal scales [2].

Among several floodplain lake systems along the lower Amazon region, the Lago Grande de Curuai (LGC) is one of the lakes subjected to the largest interseasonal changes. With a flooded area of around 3500 km² in the high water season, the LGC becomes a complex system of about 30 interconnected lakes, linked to the Amazon River by several channels [2]. when during the low water season, it shrinks to around 600 km² of open water. This complexity leads to high variability in sediment concentration across time and space in this floodplain lake system. This variability is mainly dependent on natural effects such as the hydrological basin regime, local precipitation, and floodplain geomorphology [3,4]. In addition, not only suspended sediments, but other optically active constituents such Colored Dissolved Organic Matter (CDOM) and Chlorophyll-a (Chl-a) are also co-varying in space and time [2,5] increasing optical complexity of those lake waters.

Estimates of particulate materials are fundamental for characterizing the sediment fluxes between Amazon River and the floodplains and for evaluating the impacts of climate change, LUCC and carbon exchange between the floodplains and the atmosphere [4,5] since TSS is composed of both organic and inorganic particles whose proportion and origin varies seasonally [2].

In that sense, the use of empirical and semi-analytical models based on orbital remote sensing represents a complement to *in-situ* TSS measurements since it provides a synoptic view of water bodies, giving the spatial dimension not provided by *in-situ* information. Furthermore, the new generation of Earth Observation Satellites such as Landsat 8, Sentinel 2 and CBERS-4 are apt to provide high-quality water remote sensing products. However, the development of universal algorithms is challenged by the high spatial and temporal variability in optical active constituents (OAC) among the floodplain lakes, demanding robust approaches to cope with such optical complexity. Therefore, this paper evaluates the calibration of empirical [8] and semi-analytical [9] algorithms for TSS retrievals. The Monte Carlo simulation was applied in simulated R_{rs} from Landsat-8/OLI, Sentinel-2/MSI and CBERS-4/WFI, and then, validation of these models was performed to atmospherically corrected images of these three satellites.

2. MATERIALS AND METHODS

2.1 Study Area

LGC area (Figure 1) located between Parintins-AM and Almerim-PA cities, the is representative of the lower Amazon floodplains [2,10] having been the object of many studies

[2,7]. Sediment concentrations in LGC vary in a range of 1 – 1000 mg L^{-1} from high to low water periods, respectively [2].

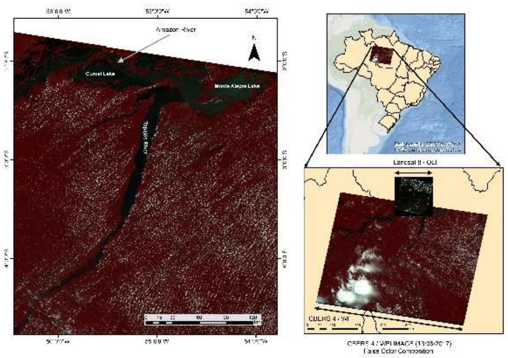

Figure 1 Study Area

2.2. Radiometric and Limnological data

The radiometric dataset was acquired using three intercalibrated TriOS Ramses spectroradiometers that operate in 400 – 900 nm range measuring Downward Irradiance (E_d), Sky Radiance (L_{sky}) and Water-Leaving Radiance (L_T) simultaneously. Remote Sensing Reflectance was calculated (Equation 1) using Mobley [9] correction for sky reflectance (ρ).

$$R_{rs} = \frac{Lt - p * L_{sky}}{E_d} \tag{1}$$

Approximated 150 spectra were acquired for each station. Initially, all spectra were visually inspected to remove obvious outliers. After that, the representative spectra for each station were selected based on the minimum sum value of the difference between median R_{rs} values at each wavelength in relation to the actual R_{rs} value at each wavelength. After spectra selection, in situ R_{rs} was used to simulate OLI, MSI and WFI spectral bands using their appropriate spectral response function (SRF) [12–14]. Total Suspended Solids (TSS) concentration was determined from samples acquired concurrently to Rrs measurements according to Wetzel and Likens [15] methodology (Table 1). All dataset was acquired in four field campaigns carried out between 2015 and 2017. A total of 94 samples of TSS and R_{rs} were used in this work.

Table 1 Mean, Minimum, Maximum, Standard Deviation (SD) and number of TSS samples in the field campaigns.

Mean TSS (mgL^{-1})	Min TSS (mgL^{-1})	Max TSS (mgL^{-1})	SD TSS (mgL^{-1})	Sample Size
32.61	5.25	235.5	31.84	94

2.3. Satellite Data

The satellite images used in this work were acquired from three earth observation satellites: Landsat 8/OLI, Sentinel 2/MSI and CBERS-4/WFI on August/2017. These images are concurently to field samples. MSI images were from 08/08, OLI images were from 10/08 and WFI images were from 11/08. The August/2017 field campaigns were carried out from Aug/08 to Aug/12. For all images, the 6S radiative transfer code [16] was applied to correct the atmosphere effects using a modified version of Py6S [17] developed at LabISA (http://www.dpi.inpe.br/labisa/) by Martins, V. and Carlos, F. The atmospheric parameters (Water Vapour, Ozone, AOT) were obtained from MODIS Level-2 atmospheric data. For OLI and MSI, a glint correction [18] were also applied.

2.4. TSS Modeling

The modeling of TSS concentrations using remote sensing techniques generally are made using empirical and semi-analytical algorithms [19]. In this work, we compare an empirical approach using a log transformation in both TSS and R_{rs} data to a the semi-analytical model formulation proposed by Nechad et al. [9] (Equation 2) re-calibrated with the *in-situ* dataset.

$$TSS = \frac{A_p * R_{rs,Bi}}{1 - R_{rs,Bi}/C_p} - B_p \tag{2}$$

Where A_p, B_p and C_p are Nechad et al. [9] coefficients for band B_i of each sensor. For calibration of both empirical and Nechad models, a Monte Carlo simulation with 10.000 repetitions was performed. At each repetition, 70% of the dataset was set apart for training and 30% for validation, resulting in 66 training samples and 28 validation samples. At each repetition both R^2 and Mean Absolute Percentage Error (MAPE) statistics were calculated to evaluate the performance of models with *in-situ* R_{rs} dataset. Then, the model parameters (i.e. slope, intercept) were obtained through the median values of the coefficients for the models. After that, the validation step was based on *in-situ* calibrated models applied to their respective atmospheric corrected images from August/2017.

3. RESULTS

3.1. Model Calibration and validation with field R_{rs}

3.1.1 Calibration with field R_{rs} for Landsat 8 / OLI

Monte Carlo simulation (Figure 2) based on field R_{rs} for OLI simulated models shows that both, Nechad and Log models presented good performance (MAPE < 30%, R^2 > 0.75). The best result was provided by Nechad model using NIR band (B5), median MAPE lower than 25% and median R^2 values > 0.85. The performance of Nechad models were better than the log models when applied to NIR bands and worse when applied to VIS bands.

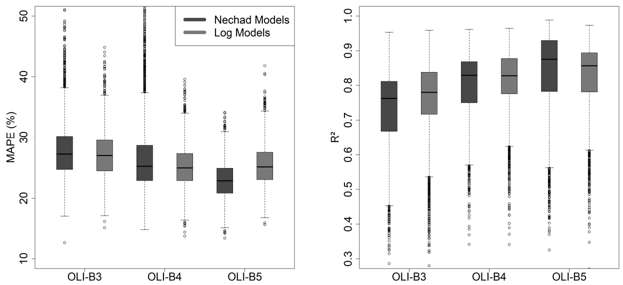

Figure 2 MAPE (Left) and R² (Right) values obtained through MC simulation for in-situ simulated R_{rs} OLI bands

3.1.2 Calibration with field R_{rs} for Sentinel 2 / MSI

Regarding Monte Carlo simulation results (Figure 3) for MSI simulated R_{rs}, they were quite similar to those observed for OLI. Better results were obtained for NIR bands (B5, B6, B7, B8) with MAPE values lower than 25% and R² higher than 0.8. The increase in correlation at higher wavelengths was also observed. MSI, as observed for OLI Nechad models, also presented better results at NIR bands and Log models presented better results at VIS bands.

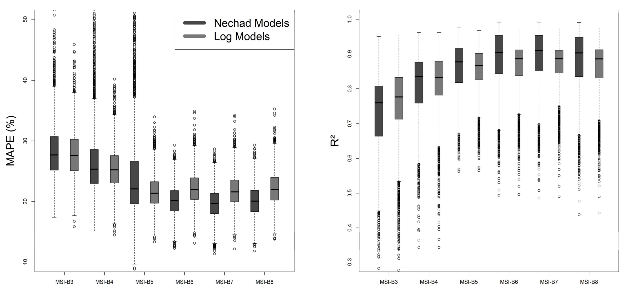

Figure 3 MAPE (Left) and R² (Right) values obtained through MC simulation for in-situ simulated R_{rs} MSI bands

3.1.3 Calibration with field R_{rs} for CBERS-4 / WFI

For the WFI Monte Carlo simulation (Figure 4) also showed results quite similar to those of OLI and MSI models, mainly for green and red bands (WFI-B3 and WFI-B4). At NIR MSI band the results were close to that of MSI B8.

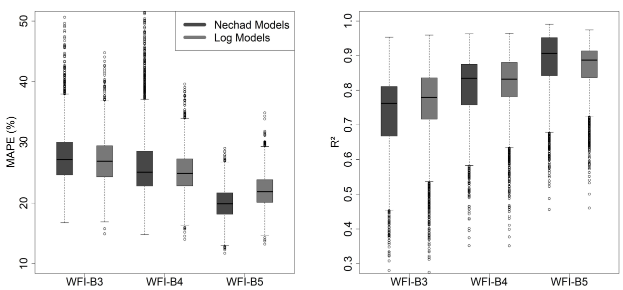

Figure 4 MAPE (Left) and R² (Right) values obtained through MC simulation for in-situ simulated R_{rs} WFI bands

3.2. Image Model Validation

The models obtained from the calibration step were applied to atmosphere corrected OLI, MSI and WFI images. The results are presented in Figure 5. Although better results for NIR bands of OLI, MSI and WFI sensors using field R_{rs}, when these models were applied to the August/2017 scene, the best results for OLI were observed for the green band for both Log and Nechad models (MAPE < 20%). Regarding MSI models, the better results were observed in models using the red-edge (B5) bands, with Log model presenting slightly better results (MAPE < 22%). Finally, for WFI the lower MAPE value was for red band (B4) (MAPE < 38%).

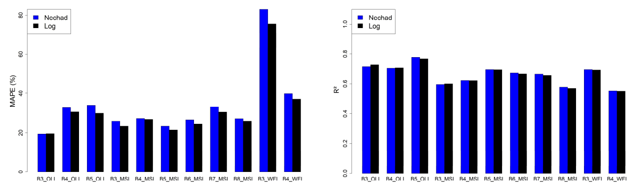

Figure 5 MAPE (Left) and R² (Right) obtained from validation in OLI, MSI and WFI scenes for August/2017.

4. DISCUSSION

The results obtained from the calibration and validation steps using *in-situ* R_{rs} dataset showed that better results for the three sensors evaluated were observed applying NIR bands. These results could be attributed to the range of TSS concentration and variability of OACs during the field campaigns. As the signal in the infrared bands is less influenced by both chlorophyll and CDOM concentration [20], the seasonal variation in the concentration of these components along the different field campaigns are minimized. In addition, R_{rs} saturation in green and red bands also impacts the visible bands causing higher errors [19]. Regarding the Log and Nechad TSS model's performance, in the VIS bands, Log models presents better results than those of Nechad. However, for NIR models, Nechad models presented better R² and MAPE values, except for the red-edge MSI B5 model. The observed results from the calibration step also show that the three sensors are similar regarding the band's performance (e.g. green and red bands) with very similar results. These close results are attributed to the similar SRF of WFI, OLI, and MSI at these bands. It is quite important this similarity among sensor's performance because helps to create virtual constellations as they provide similar errors when referred to in situ R_{rs}.

Regarding model validation in atmosphere corrected images, the three sensors provided a fair agreement with *in-situ* TSS concentration on August/2017 field campaign. However, TSS concentration for these campaign presents lower values (7 – 43.5 mgL^{-1}) results are also different from those of the models using *in-situ* R_{rs} values. For OLI image validation models, the green band presents better results. As August/2017 field campaign presents higher levels of chl-a concentration (9.34 – 67.84 μgL^{-1}), higher errors in the red band could be attributed to absorption of electromagnetic radiation in the red region of the spectrum by the Chl-a [21]. At NIR OLI band, higher errors are due to low R_{rs} signal with low TSS concentration. For MSI models, the better results are for red-edge band (B5). This band is centered at Chl-a reflectance peak (705 nm) what could be reducing the errors as TSS is a sum of inorganic and organic suspended particles, and the phytoplanktons presented in these waters contribute to backscattering [20]. WFI models present acceptable results only for the red band (MAPE < 37%). Higher errors for WFI could be attributed to uncertainties on the atmospheric correction procedure and time-lag between satellite and in-situ measurements (four days).

5. CONCLUSIONS

This study shows the applicability of TSS models and satellite data in the Amazon floodplain lake. Moreover, there is a possibility to use these sensors as a virtual constellation that improves the revisit time in the Amazon Floodplains.

6. ACKNOWLEDGMENTS

The authors thank CNPQ and CAPES for their scholarship, INPE's Remote Sensing graduate course and Brazilian Development Bank by the project (MSA-BNDES 1022114003005).

7. REFERENCES

[1] Meade, R. H. *Suspended Sediment In The Amazon River And Its Tributaries In Brazil During 1982-84*.1985.

[2] Barbosa, C. C. F. et al. Geospatial Analysis OfSpatiotemporal Patterns Of Ph, Total Suspended Sediment And Chlorophyll-A On The Amazon Floodplain. *Limnology*, Springer, V. 11, N. 2, P. 155–166, 2010.

[3] Meade, R. H. Suspended Sediments Of The Modern Amazon And Orinoco Rivers. *Quaternary International*, Elsevier, V. 21, P. 29– 39, 1994.

[4] Roddaz, M. et al. Evidence For The Control Of The Geochemistry Of Amazonian Floodplain Sediments By Stratification Of Suspended Sediments In The Amazon. *Chemical Geology*, Elsevier, V. 387, P. 101–110, 2014.

[5] Barbosa, C. C. F. et al. Metodologia De Análise Da Dinâmica De Área E Volume Inundável: O Exemplo Da Várzea Do Lago Grande De Curuaí. *Revista Brasileira De Cartografia*, V. 58, N. 3,2006.

[6] Renó, V. F. et al. Assessment Of Deforestation In The Lower Amazon Floodplain Using Historical Landsat Mss/Tm Imagery. *Remote Sensing Of Environment*, Elsevier, V. 115, N. 12, P. 3446– 3456, 2011.

[7] Moreira-Turcq, P. et al. Carbon Sedimentation At Lago Grande De Curuai, A Floodplain Lake In The Low Amazon Region: Insights Into Sedimentation Rates. *Paleogeography, Palaeoclimatology, Palaeoecology*, Elsevier, V. 214, N. 1-2, P. 27– 40, 2004.

[8] Matthews, M. W. A Current Review Of Empirical Procedures Of Remote Sensing In Inland And Near-Coastal Transitional Waters. *International Journal Of Remote Sensing*, Taylor & Francis, V. 32, N. 21, P. 6855–6899, 2011.

[9] Nechad, B.; Ruddick, K.; Park, Y. Calibration And Validation Of A Generic Multisensor Algorithm For Mapping Of Total Suspended Matter In Turbid Waters. *Remote Sensing Of Environment*, Elsevier, V. 114, N. 4, P. 854–866, 2010.

[10] Novo, E. M. L. De M. et al. Seasonal Changes In Chlorophyll Distributions In Amazon Floodplain Lakes Derived From Modis Images. *Limnology*, Springer, V. 7, N. 3, P. 153–161, 2006.

[11] Mobley, C. D. Polarized Reflectance And Transmittance Properties Of Windblown Sea Surfaces. *Applied Optics*, Optical Society Of America, V. 54, N. 15, P. 4828–4849, 2015.

[12] Barsi, J. A. et al. The Spectral Response Of The Landsat-8 Operational Land Imager. *Remote Sensing*, Multidisciplinary Digital Publishing Institute, V. 6, N. 10, P. 10232–10251, 2014.

[13] Sentinel-2 Spectral Response Functions (S2- Srf). Available At: *<Https://Earth.Esa.Int/Web/Sentinel/ User-Guides/Sentinel-2-Msi/Document-Library/-/Asset_Publisher/ Wk0tkajiisar/Content/Sentinel-2a-Spectral-Responses>*.

[14] Pinto, C. et al. First In-Flight Radiometric Calibration Of Mux And Wfi On-Board Cbers-4. *Remote Sensing*, Multidisciplinary Digital Publishing Institute, V. 8, N. 5, P. 405, 2016.

[15] Wetzel, R. G.; Likens, G. E. *Limnological Analysis*. [S.L.]: Springer Science & Business Media, 2013.

[16] Vermote, E. F. et al. Second Simulation Of The Satellite Signal In The Solar Spectrum, 6s: An Overview. *Ieee Transactions On Geoscience And Remote Sensing*, Ieee, V. 35, N. 3, P. 675–686, 1997.

[17] Wilson, R. T. Py6s: A Python Interface To The 6s Radiative Transfer Model. *Computers & Geosciences*, V. 51, N. 2, P. 166, 2013.

[18] Wang, M.; Shi, W. The NIR-SWIR Combined Atmospheric Correction Approach For Modis Ocean Color Data Processing. *Optics Express*, Optical Society Of America, V. 15, N. 24, P. 15722– 15733, 2007.

[19] Novoa, S. et al. Atmospheric Corrections And Multi-Conditional Algorithm For Multi-Sensor Remote Sensing Of Suspended Particulate Matter In Low-To-High Turbidity Levels Coastal Waters. *Remote Sensing*, Multidisciplinary Digital Publishing Institute, V. 9, N. 1, P. 61, 2017.

[20] Roesler, C. S.; Boss, E. *In Situ Measurement Of The Inherent Optical Properties (IOPs) And Potential For Harmful Algal Bloom Detection And Coastal Ecosystem Observations*. [S.L.]: Unesco Publishing, 2008. 153–206 P.

[21] Dall'olmo, G.; Gitelson, A. A. Effect Of Bio-Optical Parameter Variability And Uncertainties In Reflectance Measurements On The Remote Estimation Of Chlorophyll-A Concentration In Turbid Productive Waters: Modeling Results. *Applied Optics*, Optical Society Of America, V. 45, N. 15, P. 3577– 3592, 2006.